Bell *et al. Fluids and Barriers of the CNS* (2023) 20:51
https://doi.org/10.1186/s12987-023-00450-3

Fluids and Barriers of the CNS

RESEARCH

Open Access

Unique features of the arterial blood–brain barrier

Batia Bell[1], Shira Anzi[1], Esther Sasson[1] and Ayal Ben-Zvi[1*]

Abstract

CNS vasculature differs from vascular networks of peripheral organs by its ability to tightly control selective material exchange across capillary barriers. Capillary permeability is mostly defined by unique cellular components of the endothelium. While capillaries are extensively investigated, the barrier properties of larger vessels are understudied. Here, we investigate barrier properties of CNS arterial walls. Using tracer challenges and various imaging modalities, we discovered that at the mouse cortex, the arterial barrier does not reside at the classical level of the endothelium. The arterial wall's unique permeability acts bi-directionally; CSF substances travel along the glymphatic path and can penetrate from the peri-vascular space through arteriolar walls towards the lumen. We found that caveolae vesicles in arteriole endothelial are functional transcytosis machinery components, and that a similar mechanism is evident in the human brain. Our discoveries highlight vascular heterogeneity investigations as a potent approach to uncover new barrier mechanisms.

Keywords BBB, Arterial berrier, Super-resolution, dSTORM, Transcytosis

Introduction

Organs receive nutrients and clear metabolic waste through the blood. Vascular networks are largely assembled in a stereotypic manner in which the smallest diameter vessels (capillaries) are constructed by an inner lining of very thin endothelial cells (one or two cells in each tube section) surrounded by pericytes. The thinnest vessel wall and the very slow blood flow facilitate metabolic material exchange between the blood and the tissue. In general, arteries and veins facilitate blood supply and drainage, but each also have additional functions. Larger diameter vessels are constructed by an inner lining of endothelial cells surrounded by layers of smooth muscle (and other cell types). Arteries and their bifurcations (arterioles) function by diverging blood flow to different parts of the network by virtue of smooth muscle driven vessel constriction and dilation.

In the central nervous system (CNS), cellular processes of astrocytes (termed end-feet) construct a third layer covering each vessel. CNS vasculature also differs from peripheral organs' vascular networks in its ability to tightly control selective metabolic material exchange across capillary walls. This and additional features, such as preventing immune cells entry into the CNS, and active clearance of toxins from the tissue, are hallmarks of the blood–brain barrier (BBB) [1, 2].

The degree of capillary permeability (i.e. the ease by which blood-borne materials extravasate into the tissue) is largely set by unique cellular components of the endothelium. As such, the basic components of the BBB are continuous endothelial cells lacking fenestrations, negatively suppressing vesicular transport and constructing highly impermeable tight junctions [1, 3]. Based on tracer studies, endothelial BBB properties were assumed to exist at every level of the vascular network [1]. Nonetheless, endothelial barrier properties are mainly

*Correspondence:
Ayal Ben-Zvi
Ayalb@ekmd.huji.ac.il
[1] Department of Developmental Biology and Cancer Research, Faculty of Medicine, Hubert H. Humphrey Center for Experimental Medicine and Cancer Research, The Institute for Medical Research Israel-Canada, Hebrew University of Jerusalem, 91120 Jerusalem, Israel

investigated at the capillary level, while barrier properties of larger vessels are understudied. Moreover, even at the capillary level permeability extent is heterogeneous. This is apparent in vascular beds of circumventricular organs in which vessels are highly permeable owing to extensive fenestra, facilitating specific functions such as hormone release. It is also apparent in vascular beds with more classical barrier properties such as distinct single endothelial structures in the hippocampus, in which irregular vesicular activity facilitate an interface between the blood and neural stem cells [4]. Finally, permeability is also a dynamic feature that is being modulated along a circadian course by controlling expression levels of barrier determinants, such as in the case of multi-drug resistance transporters (ABC) in the cortex [5] or tight junction proteins in the retina [6].

Emerging evidence of endothelial heterogeneity across CNS vessel types [7] prompted us to investigate barrier properties of CNS arterial walls. We used tracer challenges and different imaging modalities and discovered that at the mouse cortical arterial wall, the BBB does not reside at the level of the endothelium. Despite relatively fast blood flow, we found non-selective penetrance of various substances from the blood, crossing both the endothelial and smooth muscle layers, but not the astrocyte end-feet layer. Arterial wall unique permeability acts bi-directionally; substances originating from the CSF can penetrate from the perivascular space, crossing the smooth muscle layer and the endothelial layer towards the vessel lumen. We show in mice, that caveolae vesicles in arteriole endothelial are functional transcytosis machinery components, and that a similar mechanism is also evident in human brain arteries.

Results

Atypical cellular barrier properties at the CNS arteriole-wall

Tracers of different sizes and molecular compositions are commonly used to test vascular permeability. We introduced tracers into the blood stream of wild-type adult mice for relatively short permeability challenges (10 min), followed by immunostaining for Neurovascular unit (NVU) components in cortical sections (endothelium, smooth muscle, astrocyte end-feet, and basement membranes). Cortical arterioles usually have a circumferential organization of a single endothelial layer, a smooth muscle layer and astrocyte end-feet, each separated by a basement membrane (Fig. 1a, illustration). We focused mostly on arterioles (of 5–10 µm diameter), but the following observations are also relevant to larger diameter cortical-penetrating arteries. With confocal microscopy imaging we found differing extents of permeability along the arteriole wall for several tracers. Albumin (70 kDa) was mostly co-localized with the endothelium (Fig. 1b). Dextran (10 kDa) signals co-localized with the endothelium and reached the smooth muscle layer, and in some cases reached beyond, up to the astrocyte end-feet (Fig. 1c). Sulfobiotin (443 Da) signals localized past the smooth muscle layer, but were confined by the outer basement membrane (Fig. 1d).

The juxtaposed organization of thin cell profiles in vessel cross-sections makes it difficult to determine precise locacalization of tracer molecules with limited imaging resolution. We therefore used super-resolution imaging (dSTORM). Precise nano-scale localization of single tracer molecules confirmed localization past both the endothelium and the smooth muscle markers of all three tracers (Fig. 2, Additional file 1: Fig. S1). Permeability quantification showed a substantial percentage of tracer molecules beyond the smooth muscle marker limits, with no significant difference between the three tracers tested (Fig. 2c). With appropriate imaging resolution, at the most abluminal location we could determine that tracers were arranged in a confined manner and did not freely disperse further into the tissue.

We conclude that unlike brain capillaries (Additional file 1: Fig. S2), the BBB in arterial walls does not reside at the level of the endothelium—in mouse CNS arteries various substances can penetrate from the blood,

(See figure on next page.)

Fig. 1 Variable degree of permeability to different tracers across the CNS arteriole-wall uncovers atypical cellular barrier properties**.** Confocal-microscopy of arteriole-wall permeability, with immunostaining for NVU components: endothelium (anti-CD31), smooth-muscle (anti-SMA), astrocyte end-feet (anti-AQP4), and basement membranes (anti-pan Laminin) of wild-type adult mouse cortical sections. **a** Schematic illustration of the experimental design: tracers of different size and molecular compositions are introduced into the blood stream and circulated for 10 min. Arteriole cross sections are used to locate fluorescent tracer signals (green circles) in the vessel wall from luminal side (blood) towards the tissue (arrow showing the path crossing the endothelial cell layer-purple, smooth-muscle layer-red each surrounded by basement membranes and all surrounded by the astrocyte end-feet) Created with BioRender.com. **b** Tracer challenges with Alexa-647 conjugated albumin for 10 min (70 kDa) demonstrating that albumin is mostly co-localized with the endothelium (arrow). **c** Challenges with Alexa-647 conjugated dextran for 10 min (10 kDa) demonstrates tracer signals co-localized with the endothelium and reaching the smooth-muscle layer (upper panel, arrow), and beyond reaching the astrocyte end-feet (lower panel, arrow). **d** Challenges with perfused sulfo-biotin (443 Da), stained with Alexa-647 conjugated streptavidin demonstrates tracer signals passed the smooth-muscle layer (upper panel, arrow), but confined by the basement membranes (lower panel, arrow). Images are representative of n = 27 arterioles profiles of n = 9 mice (3 for each tracer), Scale Bars 10 µm

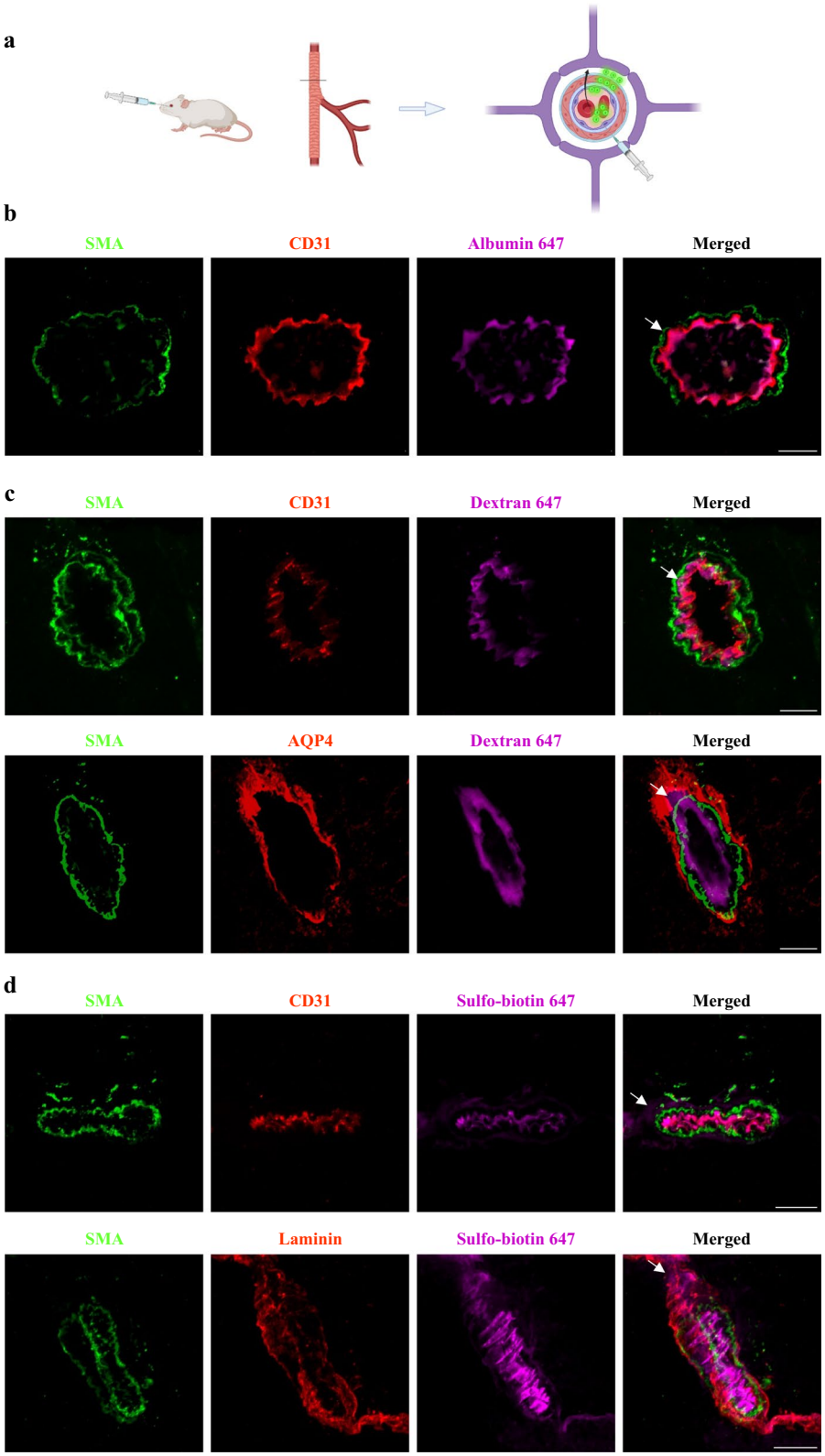

Fig. 1 (See legend on previous page.)

crossing the endothelial layer and the smooth muscle layer, but not the astrocyte end-feet layer.

Caveolae vesicles in arteriole endothelial are functional transcytosis machinery components

Recently, Chow et al. found that caveolae-vesicles in CNS arterioles mediate neurovascular coupling (arteriole constriction/dilation in response to neuronal activity) [8]. Vesicles were found in both the endothelium and the smooth muscle cells. Elegant experiments of genetic perturbations that eliminated these components revealed that only the endothelial vesicles are necessary for neurovascular coupling [8]. Since suppression of endothelial caveolae-vesicles formation is a hallmark of capillary BBB endothelium [3, 9–11] (preventing non-specific transcytosis across the barrier), we wondered if arteriole caveolae vesicles could be transcytotic components mediating the unique permeability pattern that we described. To answer this question, we used electron microscopy to image permeability challenges of two tracers: sulfo-biotin (443 Da), and horseradish peroxidase (HRP, ~ 40 kDa). Both tracers could be found in basement membranes between all three cell layers, confirming permissive permeability (Fig. 3, arrows). Abundant vesicular structures were observed in both the endothelium and the smooth muscle cells, and tracers could be found filling these vesicles (Fig. 3, arrowheads). Tracers were found in luminal and abluminal membranes pits, and in vesicles located in the cytoplasm of both cell types. Quantifying vesicular density showed significant higher vesicular density in arterial endothelium than in capillary endothelium (Fig. 3c). Smooth muscle cells exhibited abundant caveolae (flask shaped membrane pits, Fig. 3). Caveolae are involved in several muscle cell-signaling functions other than transcytosis [12]. In order to evaluate the abundance of the different structures, we compared the density of membrane pits and the density of cytoplasmic free vesicles field with both tracers (Additional file 1: Fig. S3). We found that the vesicular density was not significantly different from the caveolae density at both the luminal and the ab-luminal membranes of smooth muscle cells.

We concluded that intense vesicular activity in these cells reflects potential cargo trafficking, and therefore supports functional transcytosis machinery that underlie the unique arteriole permeability pattern.

Arterial wall permeability is bi-directional

Our electron microscopy study supports transcytosis-based permeability from the blood into the arteriole wall. Nonetheless, it could not determine the directionality of cargo movement in other axes. To address this issue, we used confocal and super-resolution imaging, this time introducing tracers into the CSF. A 'glymphatic' path describes movement of CSF from the sub-arachnoid space, along the perivascular space created between the astrocyte end-feet in the glia limitans (continuous with these covering the parenchymal side of the Pia, at the Virchow-Robin spaces of penetrating arteries) and the smooth muscle layer [13] (Fig. 4a, illustration). Adopting the methodology used to study this path [13], we injected dextran (10 kDa) tracer into the cisterna magna. First, we confirmed that tracers reached the perivascular spaces around arterioles (Fig. 4b, c, confocal microscopy), in which we could find approximate co-localization of tracers with both endothelium and smooth muscle signals. With super-resolution imaging (dSTORM), we could show precise nano-scale localization of single tracer molecules past the smooth muscle marker (Fig. 5a, arrows) and at the luminal side of the endothelium (arrowhead, the blood side). With this approach, we could see that tracers originating in the CSF compartment end up in the blood compartment across the arteriole wall. Based on tracer signal distribution, we identified tracer clusters that match the dimensions of transcytosis vesicles (Fig. 5b'). We also found vesicle-shaped structures connected to the basement membrane that resemble the ultrastructure of flask-shape membrane pits (Fig. 5b'). Therefore, we concluded that arteriole permeability is bi-directional, probably mediated also by trancytosis.

Evidence of transcytosis in human brain arterioles

The H01 dataset is a 1.4 petabyte rendering of a small sample of human brain tissue (one cubic millimeter),

(See figure on next page.)

Fig. 2 dSTORM imaging demonstrates super-resolution tracer permeability and validates the unique barrier properties of the CNS arteriole wall. Precise nano-scale localization of the sulfo-biotin tracer (443 Da), stained with Alexa-647 conjugated streptavidin. **a** Relatively low resolution TIRF mode imaging (Total Internal Reflection Fluorescence, similar to epi-fluorescence with TIRF illumination, presenting all the collected signals with no super-resolution analysis) of endothelium (anti-CD31), smooth-muscle (anti-SMA) in wild-type adult mouse brain sections, does not allow precise localization of tracer along the vascular wall due to diffraction limitation. Scale bar 10 µm. **b** dSTORM images of the same arteriole (as in **a**) shows that tracer signals are found passed both the endothelium and the smooth-muscle markers. Scale bar 10 µm. **b'**-**b"**, Inset magnifications showing distances between the tracer and the cell markers (CD31 (**b'**, SMA signal omitted) and of SMA (**b"**), scale bars **b'** 2 µm, **b"** 1 µm). **c** Quantification of tracer signals beyond the smooth muscle marker (sulfo-biotin tracer images appear here, dextran and albumin tracers images appear in Additional file 1: Fig. S1). There are no significant differences in permeability of these three tracers of different size and molecular compositions (Kruskal–Wallis H test). (L) marks the vessel lumen. Dashed arrows marks tracer direction from the lumen towards the parenchyma. Images are representative of n = 18 arteriole profiles of n = 4 mice

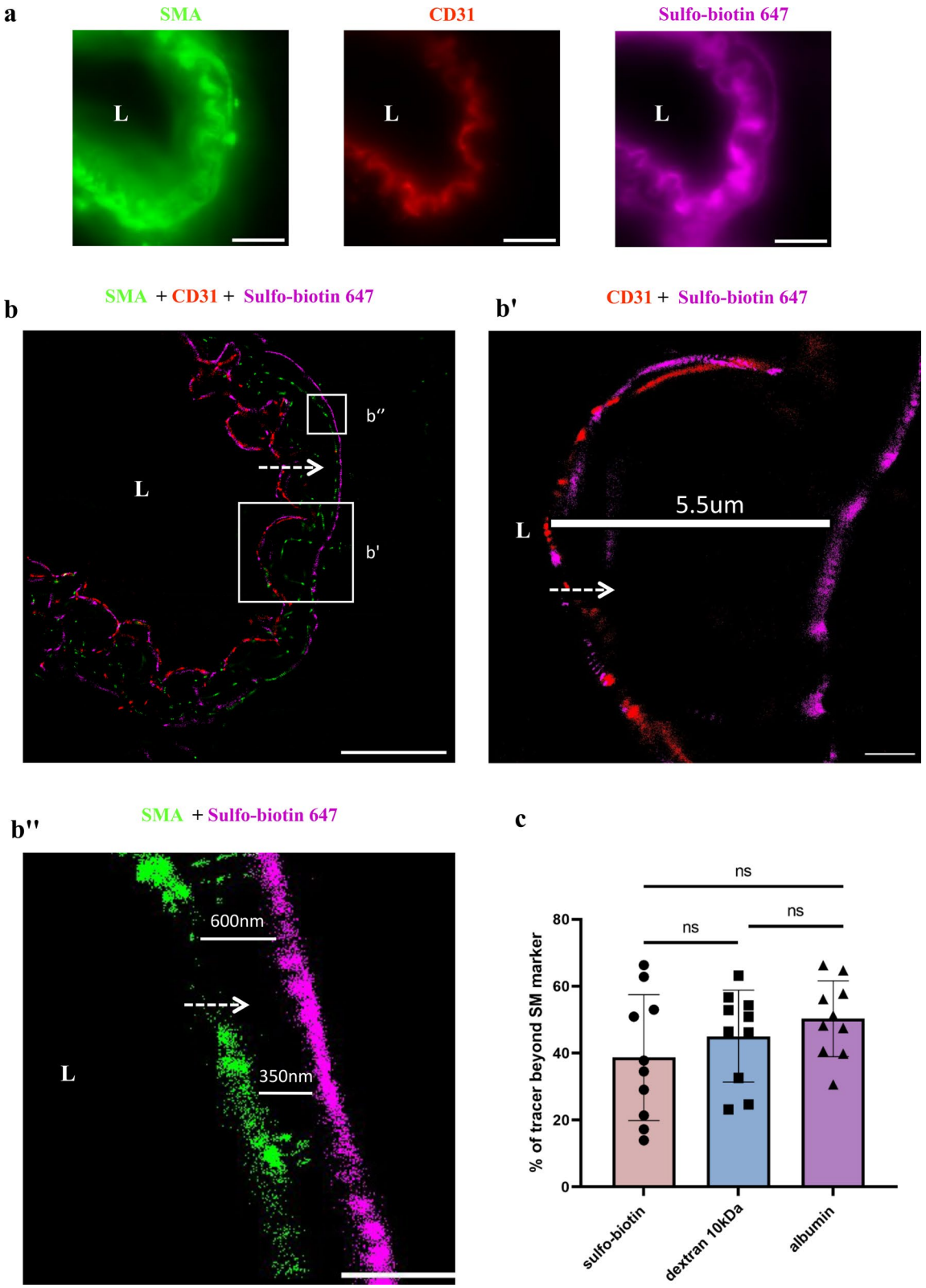

Fig. 2 (See legend on previous page.)

released by a collaboration between the Lichtman Laboratory at Harvard University and Google [14]. A rapidly preserved human surgical sample from the temporal lobe of the cerebral cortex was imaged at nanoscale-resolution by serial section electron microscopy, reconstructed and annotated by automated computational techniques [14]. We used this dataset to search for transcytosis components in human cortical vasculature. Our analysis shows that properties of the human vasculature correspond with the mouse data (Fig. 3 and previous published data [8]). In the one cubic millimeter of human temporal lobe, we found 5 arterioles. Examining these vessels along the serial section electron microscopy reconstruction, we found extensive vesicular activity in both endothelium and smooth muscle cells in patterns that resembles the mouse data. Quantifying vesicular density showed significant higher vesicular density in arterial endothelium than in capillary endothelium (Fig. 6).

Discussion

Our study reveals distinct cellular barrier properties in different segments of the CNS vascular tree. Unlike brain capillaries, the BBB in arterial walls does not reside at the level of the endothelium and various substances can penetrate from the blood, crossing the endothelium and the smooth muscles, while being restricted from crossing the astrocyte end-feet layer. It is possible that unique barrier properties of arterioles were overlooked simply because barrier properties are mostly studied at the vascular site where physiological material exchange occurs (capillaries). In this context, it is surprising that fast blood flow allows this permeability even in relatively short-term tracer challenges. Based on our current study, hyperpermeability is at least in part mediated by vesicular transport, but we cannot exclude involvement of other pathways, and future studies should also examine the possibility of unique structure and function of arteriole tight junctions.

We show here that the recently discovered caveolae vesicles in arteriole endothelial and smooth-muscle cells [8] are functional transcytosis machinery components. Vesicular activity is dependent on the expression of Cav1 (a structural vesicle component) in both cell types, but only the endothelial activity has been linked to neurovascular coupling [8]. Since we show that these vesicles carry cargo from the blood, future studies might focus on testing a possible involvement of specific cargoes in modulation of neurovascular coupling.

Other than neurovascular coupling and transcytosis, caveolae are involved in several muscle cell-signaling functions [12]. Caveolae are formed by vesicles exported form the Golgi to the cell membrane, but the abundant cytoplasmic vesicles found in our study (Additional file 1: Fig. S3) are probably not related to this biogenesis step, since they are filled with tracers. We should note that the majority of these cytoplasmic vesicles are found in areas adjacent to the cell membrane rather than being located closer to the center volume of the cells. Another experimental limitation that precludes a conclusive interpretation of smooth muscle transcytosis is the diffusion of tracers (coming from the blood side) in basement membranes between smooth muscle cells (Fig. 3 arrows). Therefore, presence of tracer at the ab-luminal side of the smooth muscle cells (facing astrocyte end-feet) could be a result of such diffusion, but might also have contribution from active transcytosis transport within the cells. Altogether, cytoplasmic free vesicles loaded with tracers at the ab-luminal fraction of the cells could be representing either endocytosis of tracer that diffused along basement membranes, or a fraction of a transcytotic processes crossing the cells from the luminal side.

At the molecular level, it is known that in capillary endothelium, the expression of *Mfsd2A* (a BBB specific lipid transporter) negatively regulates transcytosis [3, 9, 10]. Interestingly *Mfsd2A* mRNA is abundant in arteriole endothelium (yet lower than in capillary endothelium) [7], but is absent at the protein level [7, 8]. Forced transgenic *Mfsd2a* expression suppresses vesicular activity and abrogates neurovascular coupling [8].

We were fascinated by the observation that the arterial wall's unique permeability properties are bi-directional—substances originating in the CSF can penetrate from the perivascular space, crossing the smooth muscle layer and the endothelial layer towards the blood side. We found preliminary evidence that this movement is at least in part mediated by reverse transcytosis (Fig. 5). We

(See figure on next page.)

Fig. 3 Caveolae vesicles in arteriole endothelial and smooth muscle cells are functional transcytosis machinery components. HRP and sulfo-biotin tracers, imaged by TEM, demonstrate cargo trafficking in CNS arteriole cells. **a** Representative TEM image of a cortical arteriole (wild-type adult mice) following 30 min HRP tracer challenge. HRP signal is found in vessel lumen (L) as well as in basement membranes; in between the endothelial layer and smooth muscle layer (arrows), and between the smooth-muscle layer and astrocyte end-feet (arrows). Scale bar 5 µm. Inset (**a'**) ample caveolae vesicles, some of which showing HRP signals at luminal and abluminal membranes of a smooth muscle cell (arrowheads). Scale bar 500 nm. **b** Representative TEM image of perfused sulfo-biotin tracer challenge following staining with HRP conjugated streptavidin. Scale bar 5 µm. Inset (**b'**) high magnification image showing abundant tracer-field vesicles, adjacent to the abluminal membrane of a smooth-muscle cell (arrowheads). Tracer signal is found also in basement membranes (arrows). *SMC* Smooth-muscle cell, *EC* Endothelial cell, *AC* Astrocyte, *L* lumen. Scale bar 500 nm (n = 6 mice, 12 arterioles). **c** Vesicular density in mouse arterial endothelial cells compared to capillary endothelial cells. Mean vesicular density in cECs and aECs. Data are mean ± s.e.m. $^{**}p < 0.05$ (Two tailed Mann–Whitney U- test)

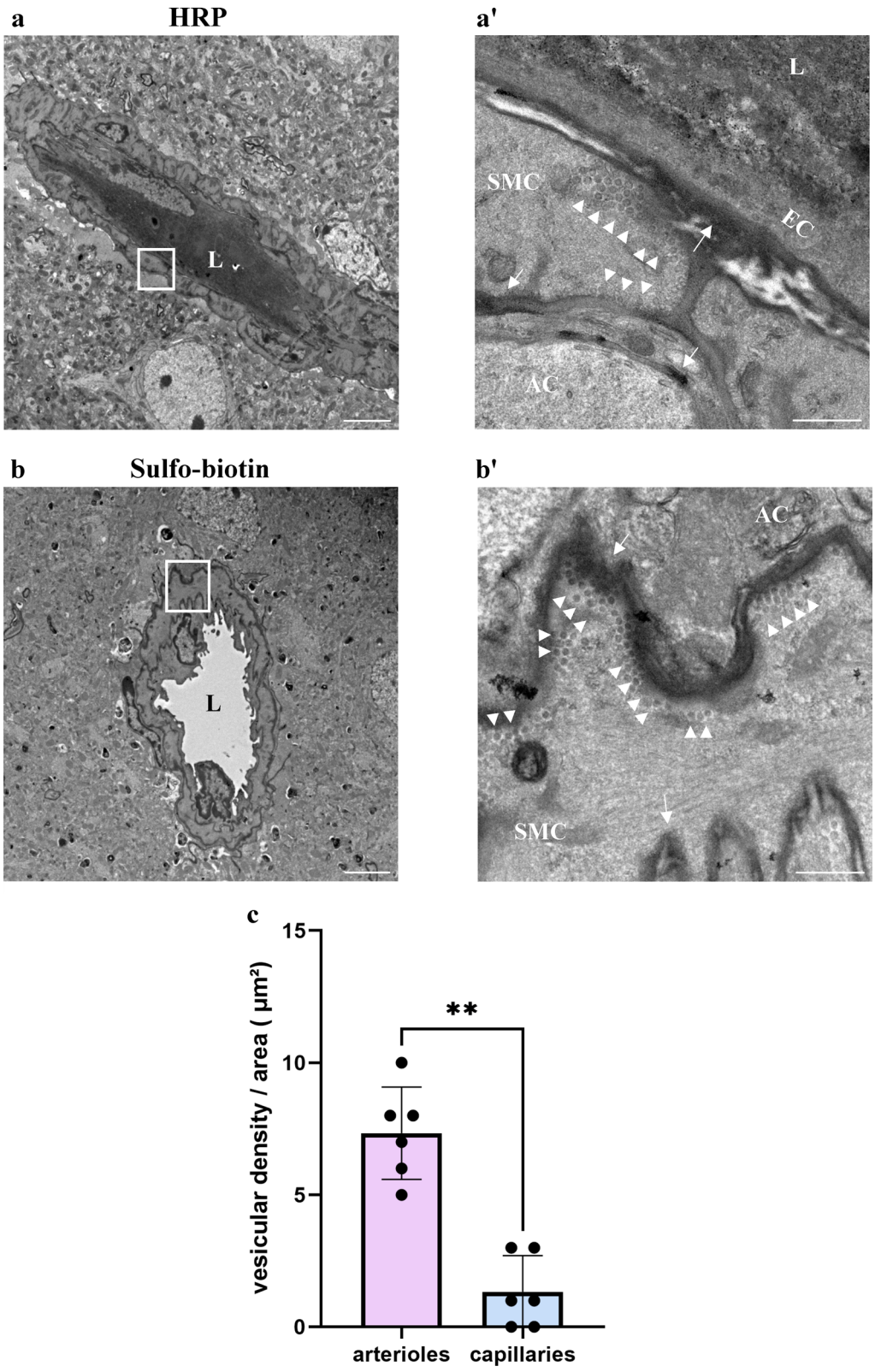

Fig. 3 (See legend on previous page.)

suggest two hypotheses for the physiological function of this phenomenon: endothelial vesicular activity is obligatory for neurovascular coupling, but as a by-product it affects barrier selectivity in arterioles. Reverse transcytosis of smooth muscle cells might have evolved in order to compensate for this non-selective leakage. Alternatively, regardless of neurovascular coupling, active reverse transcytosis mechanisms might function in the clearance of materials from the CSF into the blood. In this context, the *Intramural Peri-Arterial Drainage* pathway (IPAD) describes the location of tracers introduced in the interstitial fluid (ISF), passing from the brain parenchyma into basement membranes of capillaries and flow out of the brain along smooth muscle cell basement membranes in the walls of arteries [15–17]. IPAD supposedly involves basement membranes all around the smooth muscle cells, and diffusion between cells doesn't seem to be restricted. Altogether according to our data, accumulation of tracer (originating in the CSF) only on one side of the smooth muscle cells (luminal), might imply some kind of active directional transport that is faster than the diffusion between cells.

This unique arterial BBB structure can also be found in the human brain—arteriolar specific caveolae vesicles are evident in endothelial and smooth muscle cells of human tissue. In this analysis we observed vesicles also in other large vessels, presumably veins. Permeability and function of these structures should be explored in future studies, especially in light of the importance of veins and postcapillary venules in mediating immune cell extravasation [18]. Moreover, a recent study found that transferrin receptor-targeted liposome nano-particles for the use of drug delivery preferably exploit transport at postcapillary venules [19].

Finally, astrocyte end-feet have been suspected for many years to be anatomical counterparts of the BBB. The discovery of an endothelial barrier diminished the focus of studying atrocyte end-feet barrier functions. From an evolutionary perspective, invertebrate glia cells function as CNS barriers. Even ancestral vertebrates had glial barriers (elasmobranch fish like sharks, skates, and rays display this feature [20]). Along with the appearance of vascular systems, barrier functions shifted to the endothelium, and an endothelial barrier became dominant in all vertebrates [20]. Endothelial barrier evolution does not necessitate the degeneration of the glial barrier. Technically, it is hard to devise in vivo assays to test end-feet potential barrier functions, since blood-borne tracers are sequestered already at the capillary endothelial barrier. We show that arterioles' astrocyte end-feet layer is the last point of tracer penetrance from the blood. At this stage we have no direct evidence for cellular or molecular barrier properties of astrocytes and we are not aware of known molecular differences between arteriole and capillary associated astrocytes. Another incentive to look for such functions is that anatomically, arteriole astrocyte end-feet are glia-limitans, continuous with astrocyte end-feet covering the parenchymal side of the Pia, which possesses barrier properties. Uncovering molecular components of this putative barrier might provide new targets for drug delivery through the arterial path. We shed light on the potential of substance exchange in this previously unappreciated vascular site. Altogether we expect that the concept of a single unifying BBB will be revised, and discoveries of heterogeneity in barrier mechanisms will open new avenues for drug delivery and for better understanding the physiology of CNS vasculature.

Materials and methods

Mice

All mice were maintained in the animal facility of the Hebrew University under specific pathogen-free conditions. All animals were treated according to institutional guidelines approved by the Institutional Animal Care and Use Committee (IACUC) at Hebrew University (protocol MD-21-16361-5). 8–9 week old male and female C57BL/6JOlaHsd and ICR mice were purchased from Envigo (Rehovot, Israel).

Tissue preparation

After dissection, brains were fixed in 4% paraformaldehyde (PFA, Sigma Aldrich) at 4 °C overnight, cryopreserved in 30% sucrose and frozen in TissueTek OCT (Sakura). Frozen brains were cut to either 10 µm slices for immunofluorescence staining or 4–6 µm for dSTORM (CM1950, Leica) to produce coronal brain sections.

Immunofluorescence

10 µm thick cryo-sections were washed with phosphate buffered saline (PBS) for 5 min at room

(See figure on next page.)

Fig. 4 Tracer introduced into the CSF penetrates into the perivascular space of arteriolar wall. For testing the potential of clearance mechanisms, we adopted the methodology used to study the 'Glymphatic' path, and injected Dextran (10 kDa) into the cisterna magna. **a** Schematic illustration of the experimental design: very small volumes of tracers are introduced into the cisterna magna and circulate in the CSF for 30 min. Cortical cross sections are used to locate fluorescent tracer signals (green circles). **b** Low magnification confocal microscopy of cortical sections demonstrates expected tracer signals around arteries/arterioles (arrows, CD31 + SMA double positive vessels), but not around capillaries (arrowheads, CD31 single positive vessels). Scale bar 5 µm **c**, Confocal microscopy imaging of an arteriole cross section demonstrates approximate co-localization of the tracer with both endothelium and smooth-muscle signals (arrows). Scale bar 10 µm (n = 3 mice, 12 arterioles)

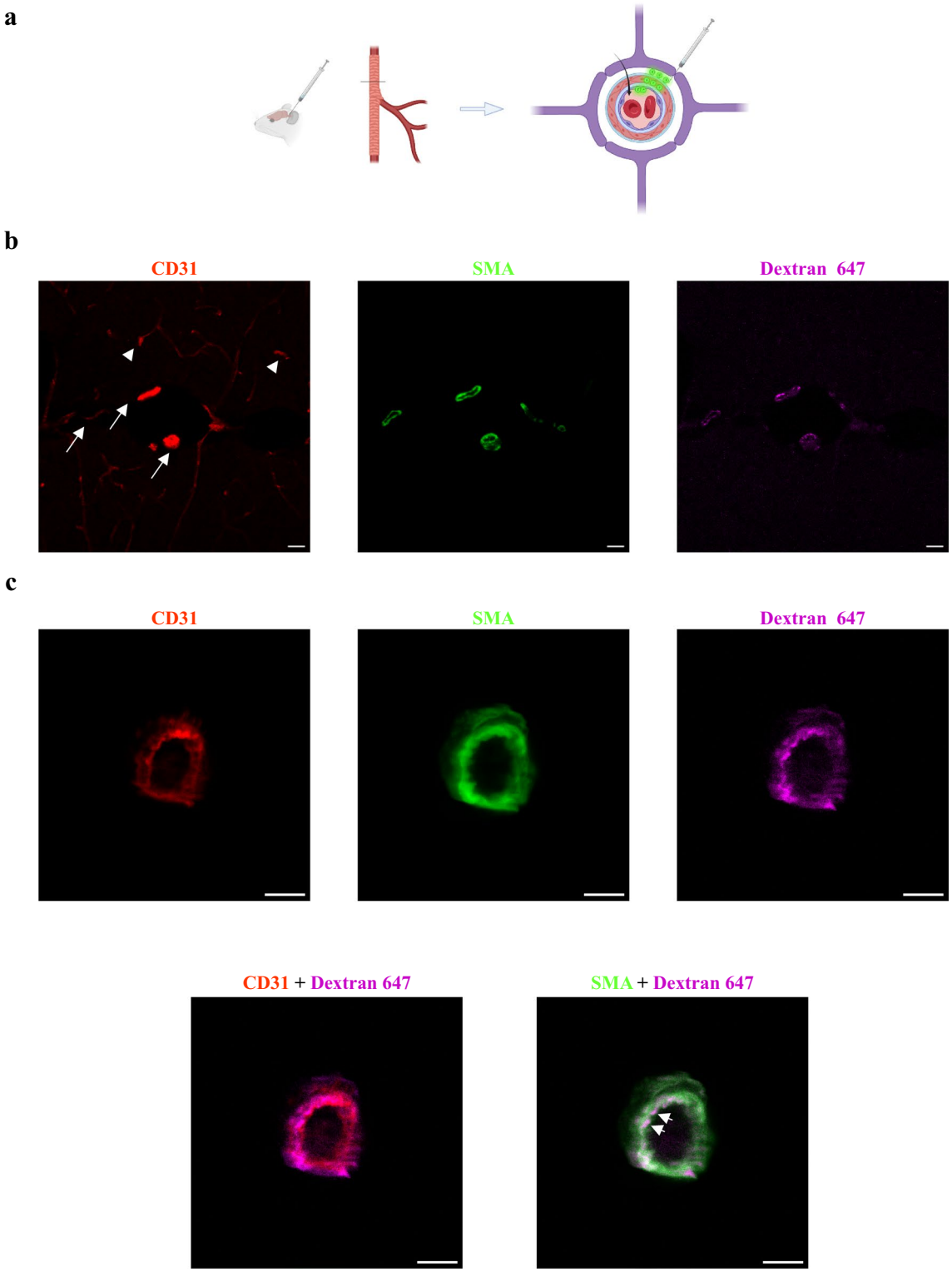

Fig. 4 (See legend on previous page.)

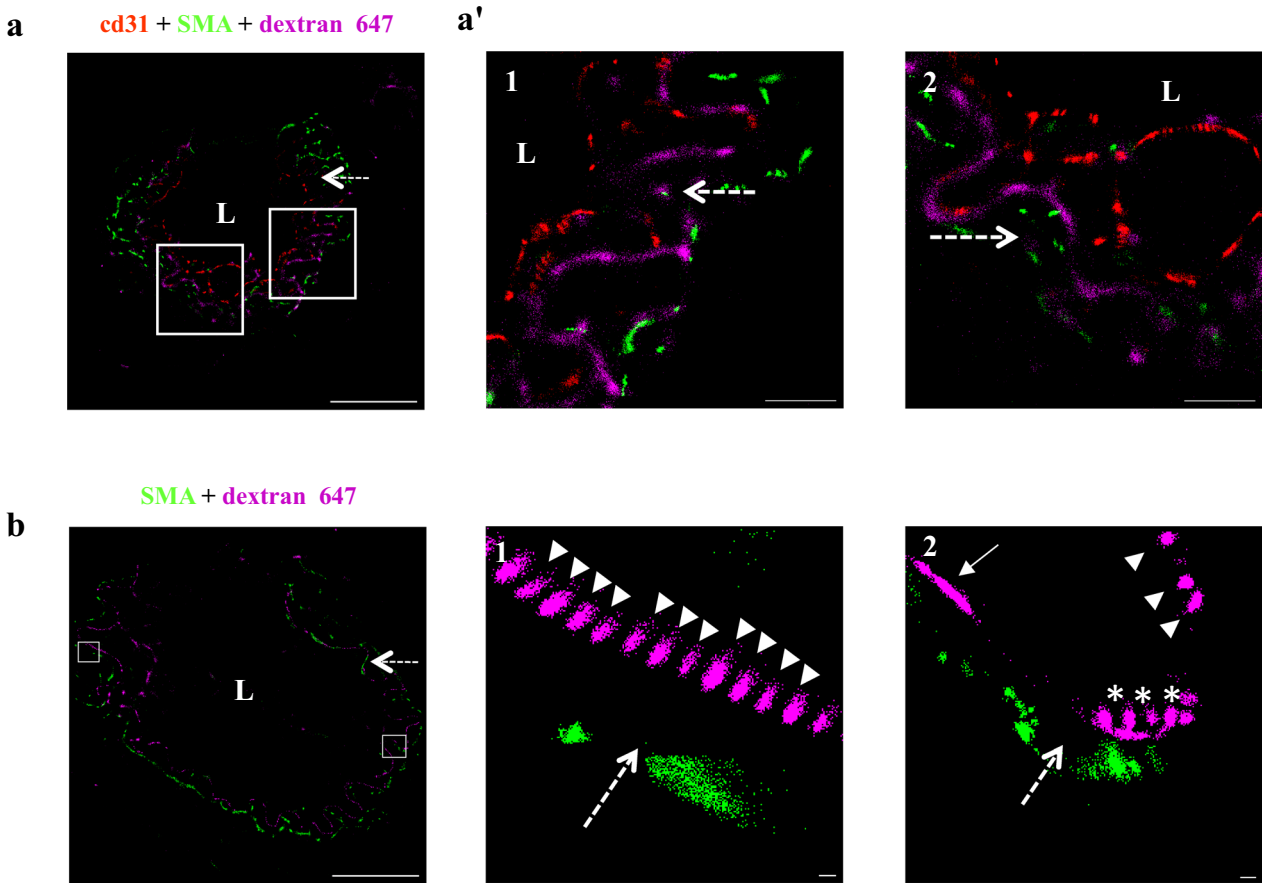

Fig. 5 Arterial wall permeability is bi-directional. Tracer introduced into the CSF travel along the Glymphatic path and can penetrate from the perivascular space across arteriolar walls towards the luminal direction. **a**, **b** 30 min CSF tracer challenges with Alexa-647 conjugated dextran (10 kDa, cisterna magna injections) and immunostaining for SMA and CD31 of wild-type adult brain sections. (L) marks the vessel lumen. Dashed arrows marks tracer direction towards the lumen. Scale bars 10 µm **a** Precise nano-scale localization with dSTORM imaging shows tracer signals located along the CSF-blood trajectory. Inset (**a'** scale bars 2 µm) magnifications demonstrating tracer signals between smooth-muscle and endothelium markers (arrows), and at the endothelium luminal side (arrowhead). **b** Based on tracer signal distribution, especially at high magnification (inset **b'** scale bars 100 nm), we identify tracer clusters that fit the dimensions of transcytosis vesicles. These vesicle-like structures are located in smooth muscle cells (arrowheads, in 1 and 2). Elongated distribution might represent tracer filled basement membrane between the smooth muscle and the endothelial cell (arrow, in 2). Vesicle-shaped structures that are connected to the basement membrane resemble the ultrastructure of flask shape membrane pits (astrix); n = 3 mice, 12 arterioles

temperature (RT) and then incubated for 3 h at room temperature (RT) with blocking solution (10% goat serum (GS), 10% horse serum (NHS), 0.05% triton X-100 in PBS). Slides were incubated with primary antibodies (diluted in 2.5% GS, 2.5% NHS, 0.05% triton X-100 in PBS) at 4 °C overnight (see antibodies table for details; Table 1). Slides were then washed with PBS, incubated with secondary antibodies for 1 h at RT and washed again. Samples were mounted with freshly made imaging buffer for dSTORM (describe

(See figure on next page.)

Fig. 6 Abundant vesicles in arteriole cells of human CNS might indicate transcytotic activity. Caveolae vesicles in arteriole endothelial and smooth muscle cells are evident in 3D EM reconstruction of human cortical tissue [14]. **a**, **b** Transmission electron microscopy images of a CNS arteriole and capillary. Pseudo-colors highlight cell types: smooth-muscle (green), endothelium (purple), pericyte (yellow), astrocyte end-foot (blue), red blood cell (red), Scale bar 10 µm. **a'**, **b'**, Magnification of the boxed area in the left panel. **a'** Abundant vesicles in aEC's (blue ovals) and aSMCs (red ovals). **c,** Example of multiple vesicles (pseudo labeled in magenta) in aSMCs. **d** Quantification showing significant higher vesicular density in aECs than in cECs (n = 5 arterioles and 5 capillaries). *SMC* Smooth-muscle cell, *EC* Endothelial cell, *AC* Astrocyte, *P* Pericyte, *L* lumen. Scale bar 1 µm. Data are mean ± s.e.m. **p < 0.05 (two tailed Mann–Whitney U- test)

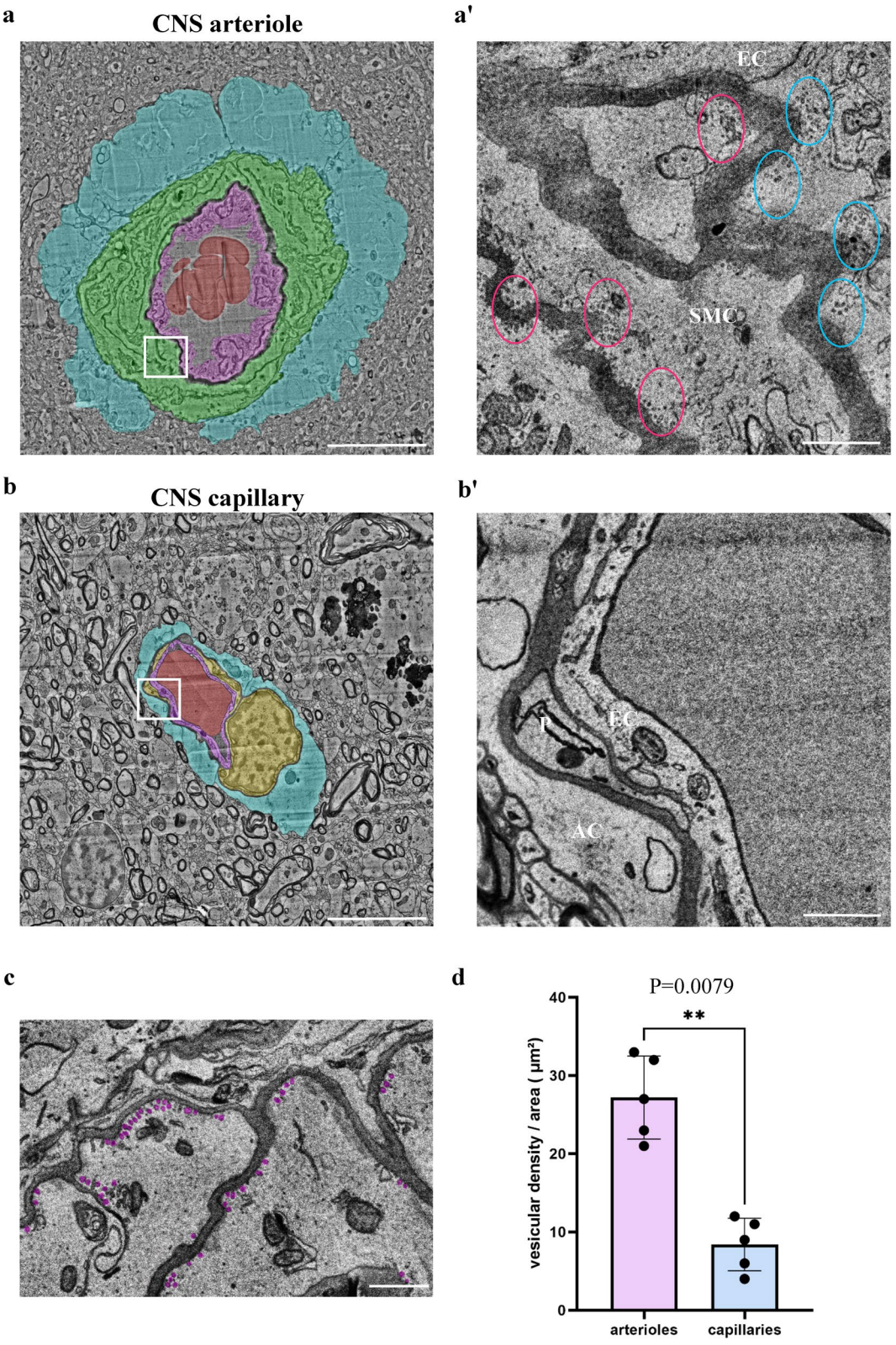

Fig. 6 (See legend on previous page.)

Table 1 Details of antibodies used

Epitope	Class	Host	Catalogue number	Company	Dilution
Actin α-smooth muscle	Monoclonal	Mouse	A-5228	Sigma-Aldrich	1:300
Aquaporin4	Polyclonal	Rabbit	AB3594	Millipore	1:400
CD31	Monoclonal	Hamster	MCA1370Z	Bio-Rad	1:50
CD31	Monoclonal	Rat	550274	BD	1:100
Laminin	Polyclonal	Rabbit	Ab11575	Abcam	1:300
TAGLN	Polyclonal	Rabbit	Ab14106	Abcam	1:300

Table 2 Details of fluorophores used

Fluorophore	Isotype	Catalogue number	Company	Dilution
Alexa fluor488	Anti-mouse IgG	715-545-151	Jackson	1:800
Alexa fluor568	Anti-rabbit IgG	A11011	Life Technologies	1:1000
Alexa fluor647	Anti-rat IgG	712-605-153	Jackson	1:1200
Atto488	Anti-mouse IgG	62197	Sigma-Aldrich	1:800
Atto488	Anti-rabbit IgG	18772	Sigma-Aldrich	1:800
CF568	Anti-mouse IgG	20105	Biotum	1:800
CF568	Anti-rabbit IgG	20098	Biotum	1:800
Streptavidin Alexa fluor647	Biotin	S32357	Molecular Probes	1:1000
Streptavidin HRP	Biotin	S911	Invitrogen	1:1000

in the dSTORM imaging section) and epifluorescence microscopy, or mounted in Fluoromount G (EMS) for confocal microscopy (Table 2).

BBB permeability assay

In all experiments, a leakage incident was defined when a tracer was localized outside the endothelial or smooth muscle cell area (indicated by marker or ultrastructure). Relative leakage index was calculated as tracer signal density (signals/area) in an arbitrary fixed area and distance from the luminal side of the relevant marker.

Dextran and albumin

Deeply anesthetized (8.5 mg/ml ketamine, 1.5 mg/ml xylazine, in 100 µl saline) 8–9 week old male and female C57BL/6JOlaHsd mice were injected retro-orbitally with 20 µl of Alexa Fluor647 anionic fixable conjugated Dextran (D22914, Molecular Probes, 4 mg/ml) or 120 µl of Alexa Fluor647 conjugated BSA (A34785, Thermo-Fisher, 5 mg/ml). The tracer was allowed to circulate for 10 min. Brains were dissected and handled as described under tissue preparation section.

NHS-biotin

Deeply anesthetized 8–9 week old male and female C57BL/6JOlaHsd mice were perfused for 5 min with sulfo-NHS-biotin (4 mg/20 g mouse body weight, Thermo Scientific, cat no. 21217, dissolved in 20 ml PBS). Brains were dissected and handled as described under tissue preparation section.

HRP

Deeply anesthetized 8–9 week old male and female ICR mice were injected retro-orbitally with 0.4 ml of HRP (Sigma Aldrich, HRP type II, 10 mg/20 g mouse body weight, dissolved in PBS). After 30 min of HRP circulation, brains were dissected and fixed as described in the TEM section.

Intracisterna magna (i.c.m.) injection

Mice were anesthetized with ketamine/medetomidine i.p. and injected i.c.m. into the cisterna magna with 2 µl of Dextran, Alexa Fluor647 anionic, fixable (D22914, Molecular Probes, 4 mg/ml). Mice were then left on a heating pad for 30 min before brains were dissected and handled as described in the tissue preparation section.

Transmission electron microscopy (TEM)

Freshly dissected tissue samples were fixed with Karnovsky's fixative (2% PFA, 2.5% glutaraldehyde in 0.1 M cacodylate buffer, pH = 7.4) for 4 h at RT, followed by a 1:2 dilution of Karnovsky's fixative in 0.1 M cacodylate buffer overnight at 4 °C. Sections of 60–80 nm were cut on Leica vibrating blade microtome (VT1000S), and developed with DAB. For 3,3′-Diaminobenzidine (DAB) staining, sections were incubated in 0.05 M Tris–HCl buffer (pH 7.6) containing 5 mg 3–3′ diaminobenzidine (Thermo Scientific, TA-060-HDX) per 10 mL buffer and a final concentration of 0.01% hydrogen peroxide for 15 min at RT. The DAB reaction was stopped with PBS wash and quenched by post fixation in 2% osmium tetroxide sodium cacodylate buffer (OsO_4). Samples were post-fixed in 1%OsO_4 in 0.1 M cacodylate buffer for 2 h, dehydrated in a graded series of alcohols, and embedded in epoxy resin. Sections of 60–80 nm were cut on an ultramicrotome (Ultracut, Reichert-Jung) contrasted with uranyl acetate and lead citrate, and examined with a Jeol (JEM-1400 PLUS, Japan) electron microscope.

Fluorescence microscopy

Immunofluorescence images were captured using the following confocal microscopes: Nikon Eclipse Ni, objective × 20 and × 40 with a Nikon C2 camera, and Nis-Elements software, or with Nikon TE-2000, objective × 20, × 40 and × 60 with EZ-C1 software.

dSTORM imaging

We used a dSTORM (direct stochastic optical reconstruction microscopy) system, which allows imaging at approximately 20 nm resolution by using photo-switchable fluorophores (all dSTORM imaging was done on TIRF mode). 4–6 µm brain slices were mounted on poly-D-lysine coated coverslips (no. 1.5 H, Marienfeld-superior, Lauda-Königshofen, Germany). dSTORM imaging was performed in a freshly prepared imaging buffer containing 50 mM Tris (pH 8.0), 10 mM NaCl and 10% (w/v) glucose with an oxygen-scavenging GLOX solution (0.5 mg/ml glucose oxidase (Sigma-Aldrich)), 40 µg/ml catalase (Sigma-Aldrich), 10 mM cysteamine MEA (Sigma-Aldrich), and 1% β mercaptoethanol (Barna et al., 2016; Dempsey et al., 2011; Zhang et al., 2016) [21–23]. A Nikon Ti-E inverted microscope was used. The N-STORM (Nikon STORM system) was built on TIRF illumination using a 1.49 NA X100 oil immersion objective and an ANDOR DU-897 camera. 488, 568 and 647 nm laser lines were used for activation with cycle repeat of ~ 8000 cycles for each channel. Nikon NIS Element software was used for acquisition and analysis; analysis was also performed by ThunderSTORM (NIH ImageJ [Ovesný et al., 2014] [24]).

dSTORM quantifications

The dSTORM approach we used is based on labeling the target protein with a primary antibody and then using a secondary antibody conjugated to a fluorophore. Thus, resolved signals represent a location that is approximately 40 nm from the actual epitope (assuming the approximation of the two antibodies' length in a linear conformation). The number of signals represents an amplification of the actual target numbers. Amplification corresponds to the primary antibody in the case of a polyclonal antibody (assuming binding to several epitopes in the same protein, which could be reduced by the use of monoclonal antibodies). Amplification also corresponds to several secondary antibodies binding to a single primary antibody and to several fluorophores attached to a single secondary antibody. Nevertheless, resolution of approximately 20 nm allows us to separate signals and to use these as proxies to the abundance of target molecules, which can reliably be used to compare different states [4, 25].

Single molecule localization microscopy (SMLM) results in point patterns having specific coordinates of individual detected molecules. These coordinates are typically summarized in a 'molecular list' (provided by ThunderSTORM analysis (NIH ImageJ) [Ovesný et al., 2014] [24]).

Statistical analysis

All comparisons were performed by two-tailed Mann–Whitney U- tests, (as indicated in the figure legends), for multiple comparisons Kruskal–Wallis H test was used, $p < 0.05$ was considered significant. (GraphPad Prism 8.0.1 [244] for Windows, GraphPad Software, San diego, California, USA).

Supplementary Information

The online version contains supplementary material available at https://doi.org/10.1186/s12987-023-00450-3.

Additional file 1: Figure S1. dSTORM imaging demonstrates super-resolution tracer permeability, validating unique barrier properties of the CNS arteriole-wall. Adult wild-type mouse cortical sections stained with SMA and imaged in dSTORM following tracer injections. Both albumin signals (**a**) and dextran signals (**b**) are found passed SMA markers. (L) marks the vessel lumen. Dashed arrows marks tracer direction from the lumen towards the parenchyma. Scale bar 10 µm (n = 6 mice, 24 arterioles). Quantification is shown in Fig. 2c. **Figure S2.** dSTORM imaging demonstrates super-resolution tracer permeability, confirming endothelial barrier properties of CNS capillaries. dSTORM imaging of wild-type adult mouse cortical capillaries, following tracer challenges from the blood (retro-orbital injections), (L) marks the lumen. Sections were stained for an endothelial marker (CD31). Tracer challenge demonstrates that all three tracers are mostly co-localized with CD31 (**a,** albumin 647 (70 kDa), **b**, dextan 647 (10 kDa), and **c,** sulfo-biotin 647 (443 Da)). Scale Bar 10 µm (n = 9 mice, 27 capillaries). **Figure S3.** Vesicle density in mouse arterial smooth muscle cells. Quantification comparing mean density of caveolae (membrane pits) and cytoplasmic free vesicles in areas adjacent to the luminal and ab-luminal membranes. Analysis corresponds to imaging

presented in Fig. 3, of experiments with sulfo-biotin (**a**) or HRP (**b**) tracer challenges from the blood (retro-orbital injections). Data are mean ± s.e.m. *p < 0.05 (Two tailed Mann–Whitney U- test, n = 5 smooth muscle cells TEM profiles).

Acknowledgements
We would like to thank; the Ben-Zvi group for scientific inputs, Dr. Evellina Sjostedt and Dr. Yaron Meirovitch for scientific inputs and guidance with the H01 dataset analyses, Gillian Kay for scientific editing, the electron microscopy units (intra-departmental core facility at the Hebrew University Medical School and the Alexander Silberman Institute of Life Sciences) for technical support.

Author contributions
BB and ABZ conceived the project and designed the experimental plan. BB performed the experiments, analyses data and prepared the figures. SA and ES assisted and instructed in some of the experiments. BB and ABZ wrote the manuscript with SA and ES reviewing and contributing to the writing. All authors read and approved the final manuscript.

Funding
This study was supported by the Leona M. and Harry B. Helmsley Charitable Trust (2015PG-ISL007); and the Israel Science Foundation (grants 1882/16 and 2402/16) to ABZ.

Availability of data and materials
All data generated or analyzed during this study are included in the manuscript and supporting files. Any additional images of interest or different image formats (such as Tiff and ND2 images and CSV files for dSTORM imaging) could be provided upon request to the corresponding author.

Declarations

Ethics approval and consent to participate
No human subjects participated in this study. Data of the human brain sample of the H01 dataset was released by a collaboration between the Lichtman Laboratory at Harvard University and Google [14], and our analysis follows ethics approval of this study. All animals were treated according to institutional guidelines approved by the Institutional Animal Care and Use Committee (IACUC) at Hebrew University (protocol MD-21-16361-5).

Consent for publication
Not applicable since no human subjects participated in this study. All authors approved the publication.

Competing interests
The authors declare no competing interests**.**

Received: 11 December 2022 Accepted: 5 June 2023
Published online: 27 June 2023

References

1. Reese TS, Karnovsky MJ. Fine structural localization of a blood-brain barrier to exogenous peroxidase. J Cell Biol. 1967;34:207–17. https://doi.org/10.1083/jcb.34.1.207.
2. Langen UH, Ayloo S, Gu C. Development and cell biology of the blood-brain barrier. Annu Rev Cell Dev Biol. 2019;35:591–613. https://doi.org/10.1146/annurev-cellbio-100617-062608.
3. Ben-Zvi A, et al. Mfsd2a is critical for the formation and function of the blood-brain barrier. Nature. 2014;509:507–11. https://doi.org/10.1038/nature13324.
4. Licht T, et al. Hippocampal neural stem cells facilitate access from circulation via apical cytoplasmic processes. Elife. 2020. https://doi.org/10.7554/eLife.52134.
5. Pulido RS, et al. Neuronal activity regulates blood-brain barrier efflux transport through endothelial circadian genes. Neuron. 2020;108:937-952.e937. https://doi.org/10.1016/j.neuron.2020.09.002.
6. Hudson N, et al. Dysregulated claudin-5 cycling in the inner retina causes retinal pigment epithelial cell atrophy. JCI Insight. 2019. https://doi.org/10.1172/jci.insight.130273.
7. Vanlandewijck M, et al. A molecular atlas of cell types and zonation in the brain vasculature. Nature. 2018;554:475–80. https://doi.org/10.1038/nature25739.
8. Chow BW, et al. Caveolae in CNS arterioles mediate neurovascular coupling. Nature. 2020;579:106–10. https://doi.org/10.1038/s41586-020-2026-1.
9. Andreone BJ, et al. Blood-brain barrier permeability is regulated by lipid transport-dependent suppression of caveolae-mediated transcytosis. Neuron. 2017;94:581-594.e585. https://doi.org/10.1016/j.neuron.2017.03.043.
10. O'Brown NM, Megason SG, Gu C. Suppression of transcytosis regulates zebrafish blood-brain barrier function. Elife. 2019. https://doi.org/10.7554/eLife.47326.
11. Ayloo S, Gu C. Transcytosis at the blood-brain barrier. Curr Opin Neurobiol. 2019;57:32–8. https://doi.org/10.1016/j.conb.2018.12.014.
12. Parton RG, Simons K. The multiple faces of caveolae. Nat Rev Mol Cell Biol. 2007;8:185–94. https://doi.org/10.1038/nrm2122.
13. Iliff JJ, et al. Cerebral arterial pulsation drives paravascular CSF-interstitial fluid exchange in the murine brain. J Neurosci. 2013;33:18190–9. https://doi.org/10.1523/jneurosci.1592-13.2013.
14. Shapson-Coe A, et al. A connectomic study of a petascale fragment of human cerebral cortex. BioRxiv. 2021. https://doi.org/10.1101/2021.05.29.446289.
15. Albargothy NJ, et al. Convective influx/glymphatic system: tracers injected into the CSF enter and leave the brain along separate periarterial basement membrane pathways. Acta Neuropathol. 2018;136:139–52. https://doi.org/10.1007/s00401-018-1862-7.
16. Arbel-Ornath M, et al. Interstitial fluid drainage is impaired in ischemic stroke and Alzheimer's disease mouse models. Acta Neuropathol. 2013;126:353–64. https://doi.org/10.1007/s00401-013-1145-2.
17. Carare RO, et al. Solutes, but not cells, drain from the brain parenchyma along basement membranes of capillaries and arteries: significance for cerebral amyloid angiopathy and neuroimmunology. Neuropathol Appl Neurobiol. 2008;34:131–44. https://doi.org/10.1111/j.1365-2990.2007.00926.x.
18. Jeong HW, et al. Single-cell transcriptomics reveals functionally specialized vascular endothelium in brain. Elife. 2022. https://doi.org/10.7554/eLife.57520.
19. Kucharz K, et al. Post-capillary venules are the key locus for transcytosis-mediated brain delivery of therapeutic nanoparticles. Nat Commun. 2021;12:4121. https://doi.org/10.1038/s41467-021-24323-1.
20. Bundgaard M, Abbott NJ. All vertebrates started out with a glial blood-brain barrier 4–500 million years ago. Glia. 2008;56:699–708. https://doi.org/10.1002/glia.20642.
21. Barna L, et al. Correlated confocal and super-resolution imaging by VividSTORM. Nat Protoc. 2016;11:163–83. https://doi.org/10.1038/nprot.2016.002.
22. Dempsey GT, Vaughan JC, Chen KH, Bates M, Zhuang X. Evaluation of fluorophores for optimal performance in localization-based super-resolution imaging. Nat Methods. 2011;8:1027–36. https://doi.org/10.1038/nmeth.1768.
23. Zhang J, Carver CM, Choveau FS, Shapiro MS. Clustering and functional coupling of diverse ion channels and signaling proteins revealed by super-resolution STORM microscopy in neurons. Neuron. 2016;92:461–78. https://doi.org/10.1016/j.neuron.2016.09.014.
24. Ovesný M, Křížek P, Borkovec J, Svindrych Z, Hagen GM. ThunderSTORM: a comprehensive ImageJ plug-in for PALM and STORM data analysis and super-resolution imaging. Bioinformatics. 2014;30:2389–90. https://doi.org/10.1093/bioinformatics/btu202.
25. Sasson E, et al. Nano-scale architecture of blood-brain barrier tight-junctions. BioRxiv. 2021. https://doi.org/10.1101/2021.08.12.456150.

Publisher's Note